Arrest stress of uniformly sheared wet granular matter

S. H. Ebrahimnazhad Rahbari

Department of Physics, Plasma and Condensed Matter Computational Laboratory,
Faculty of Sciences, Azarbaijan Shahid Madani University, 51745-406 Tabriz, Iran

M. Brinkmann

Max-Planck-Institut für Dynamik und Selbstorganisation (MPI DS), 37077 Göttingen, Germany and
Experimental Physics, Saarland University, 66123 Saarbrücken

J. Vollmer

Max-Planck-Institut für Dynamik und Selbstorganisation (MPI DS), 37077 Göttingen, Germany and
Fakultät für Physik, Universität Göttingen, 37077 Göttingen, Germany
(Dated: June 23, 2015)

We conduct extensive independent numerical experiments considering frictionless disks without internal degrees of freedom (rotation etc.) in two dimensions. We report here that for a large range of the packing fractions below random-close packing, all components of the stress tensor of wet granular materials remain finite in the limit of zero shear rate. This is direct evidence for a fluid-to-solid arrest transition. The offset value of the shear stress characterizes plastic deformation of the arrested state which corresponds to *dynamic yield stress* of the system. Based on an analytical line of argument, we propose that the mean number of capillary bridges per particle, ν, follows a non-trivial dependence on the packing fraction, ϕ, and the capillary energy, ε. Most noticeably, we show that ν is a generic and universal quantity which does not depend on the driving protocol. Using this universal quantity, we calculate the arrest stress, σ_a, analytically based on a balance of the energy injection rate due to the external force driving the flow and the dissipation rate accounting for the rupture of capillary bridges. The resulting prediction of σ_a is a non-linear function of the packing fraction ϕ, and the capillary energy ε. This formula provides an excellent, parameter-free prediction of the numerical data. Corrections to the theory for small and large packing fractions are connected to the emergence of shear bands and of contributions to the stress from repulsive particle interactions, respectively.

I. INTRODUCTION

Careful studies for dry granular materials suggest that the arrest of granular flow is universal in the sense that this non-equilibrium transition admits a continuum description. This points to the existence of an equation of state for dry granular matter [1–6]. Similarly, various features of phase transition in vertically agitated wet granular materials can faithfully be described in terms of thermodynamic concepts [7–11].

Recently, a number of papers [12–16] also addressed phase transitions in sheared wet granular matter. In particular, the arrest of wet granular flows driven by external forces with a cosine profile was attributed to a crossover of the power injected into the flow by the external field and the power dissipated in the rupturing of capillary bridges [12, 15, 16].

This provided a quantitative description of the arrest of shear flows of bidisperse disks [12] and dumbbells [16] with a fixed density, and of three-dimensional gravity-confined flow of monodisperse grains [15]. The studies established that the minimal external forcing required to maintain flow can be calculated along the same line for transitions in fixed-density and fixed-pressure settings. Also, for both wet disks and dumbbells, a large hystere-

sis was identified in which the fluid-to-solid arrest stress, σ_a, or the dynamic yield stress, has been found to be smaller than the solid-to-fluid yield stress, or the static yield stress. This is in accord with the conventional wisdom where the stress at yield point is conceived to be larger than the minimum (plastic) stress which is required to maintain the flow. Moreover, in a recent study, the difference of the static and dynamic yield stress is pinned down to the nonmonotonicity of the flow curves. Furthermore, it was shown that the nonmonotonicity of the flow curves indicates a shear banding instability [17].

Here, we augment these studies by addressing the arrest stress in systems with a prescribed global shear rate, $\dot{\gamma}$. Rather than settings with complex flow profiles we consider for our present study uniform shear flows in a Lees-Edwards [18, 19] periodic boundary flow geometry (Fig. 1). This point of view is dual to the study of force-controlled systems where we prescribe a force amplitude and measure the minimal force required to sustain flow. In the present study we will address the arrest stress, *i.e.,* the smallest value of the stress observed when decreasing the shear shear rate in spatially uniform granular flows. By definition of the stress tensor, the product of this arrest stress and the system size amounts to the minimal force that creeping flows with uniform
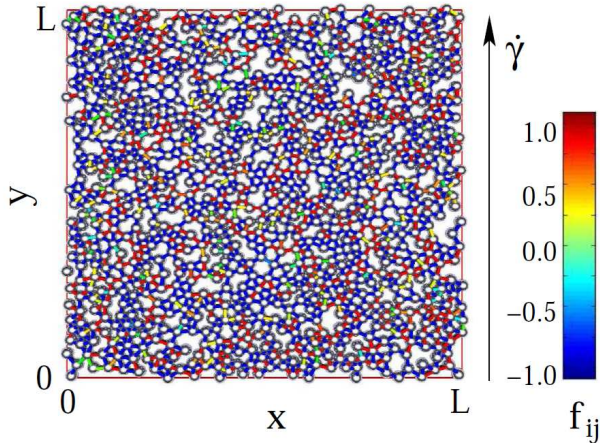
FIG. 1: (color online) Setup of the simulations with a snapshot of the system. It comprises of a square box of length L sheared in vertical direction with a shear rate, $\dot{\gamma}$, and Lees-Edwards (skew periodic) boundary conditions. Disks are indicated by circles that represent their actual size. The strength of the forces, f_{ij}, acting between the disks i and j is indicated by lines connecting the disks, where the color marks the strength of the force according to the color bar to the left. On the color palette, negative (positive) numbers correspond to attractive (repulsive) force. The snapshot shows a uniformly sheared state of a simulation of size, $L = 30$, shear rate, $\dot{\gamma} = 0.03$, and capillary-bridge energy, $\varepsilon = 0.05$, and packing density of disks, $\phi = 0.8$.

shear profile exert on the borders of a shear cell. This correspondence provides a quantitative prediction of the arrest stress where the only adjustable parameters have been measured in the force-controlled setting [12]. The agreement provides further support for the modeling of the flow threshold based on energy dissipation arguments that were established in [12, 15].

The present study is based on extensive simulations of a two dimensional wet granular material whose critical force for the arrest of flow has fully been characterized in Ref. [12]. In contrast to that previous work we address now Lees-Edwards shear flow. We determine the dependence of the arrest stress, σ_a, on the packing density, ϕ, and the capillary energy, ε.

The data are obtained by careful extrapolation of a sequence of numerical measurements of the stress for larger shear rates to vanishing $\dot{\gamma}$, where we take care to base this extrapolation only on systems with uniform shear profiles. Requiring consistency with the setting where the flow is driven by an external force [12], provides a parameter-free prediction of σ_a that is in excellent quantitative agreement with the numerical results.

The paper is organized as follows: In Sect. II we revisit the theory for the arrest of flow [12], and adapt it to describe the arrest stress of a uniformly sheared system. Subsequently, in Sect. III, we describe our system, its equations of motion, the approach adopted to solve them numerically, and the data analysis. Sect. IV comprises the results on the shear-rate dependence of the stress, and its extrapolation to zero shear rate. We will demonstrate that for intermediate packing densities, ϕ, the parameter dependence of the arrest stress is faithfully described by the parameter free prediction derived in Sect. II, and trace down the additional physical processes causing the differences for small and large ϕ. Our main results are summarized in Sect. V.

II. PREDICTING THE ARREST STRESS

We consider uniform shear in a two-dimensional system in a domain of size $L \times L$. By definition, the shear stress, σ_{xy}, corresponds to a force $\sigma_{xy}L$ required to act at the boundaries of the system in order to maintain the uniform flow. Following [12] we identify the critical force persisting at very small shear rates based on a power balance of the work injected into, and dissipated in the system. Energy is dissipated by breaking capillary bridges spanning the stress network. Hence, the dissipated power takes the form

$$\langle P_{\text{diss}} \rangle = \int_0^L dx \, n_s(x) \left| \frac{dv_y(x)}{dx} \right| \nu\varepsilon = N \, \dot{\gamma} \, \nu\varepsilon \qquad (1)$$

where ε is the energy needed to rupture a capillary bridge, and ν the average number of bridges ruptures when two disks pass in the shear flow. To arrive at the flow configuration (i) the spatial density of disks, $n_s(x)$, per unit length is the ratio of the total number of disks, N, and the width, L, of the system, and (ii) the shear rate is constant, $dv_y(x)/dx = \dot{\gamma}$ =const.

On the other hand, for a system with uniform density and shear the total injected power is the product of the off-diagonal element of the stress tensor, σ_{xy}, the shear rate, $\dot{\gamma}$, and the system area, L^2,

$$\langle P_{\text{forcing}} \rangle = \sigma_{xy} \, \dot{\gamma} \, L^2 \,. \qquad (2)$$

Flow ceases when the forcing injects too little energy to balance dissipation. The threshold value, σ_a, is obtained by balancing $\langle P_{\text{diss}} \rangle$ and $\langle P_{\text{forcing}} \rangle$,

$$\sigma_a = n_a \, \nu\varepsilon \qquad (3)$$

where $n_a = N/L^2$ is the areal density of disks.

In this expression the number ν depends on the packing fraction, ϕ, and on the capillary energy, ε, because collective motion is needed when disks pass each other in a dense system—as initially discussed for a system where flow is driven by an external cosinus-shaped force field [12]. In Ref. [12], based on systematic data collapses and heuristic scaling arguments, we have derived an explicit analytical formula for the dependence of the average bridge number, ν, on the packing fraction, ϕ, and the capillary energy, ε. As an alternative equation,
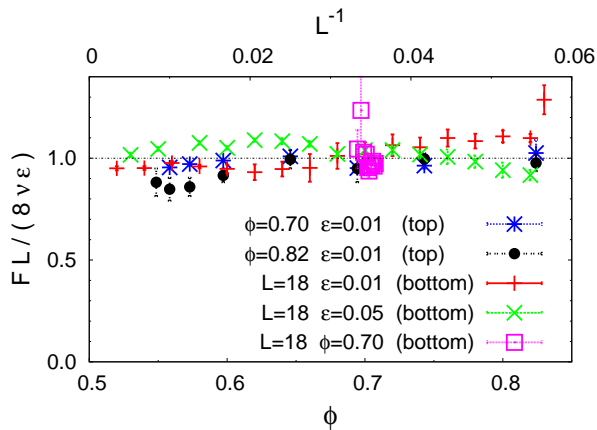
FIG. 2: (color online) Fit of the amplitude, F, of the critical cosinus force field required to maintain a flow in periodic boundary conditions. In Ref. [12] it was shown that $F = 8\varepsilon\nu/L$, and we show here that the numerical data discussed in that paper are well described by the expression, Eq. (4), for ν. The data shown by stars and filled circles refer to simulations at fixed $\varepsilon = 0.01$ and packing densities $\phi = 0.7$ and 0.82, respectively, where we varied the system size L as indicated by the top axis of the graph. The data shown by pluses and crosses show results of simulations for a systems size $L = 18$, capillary energies $\varepsilon = 0.01$ and 0.05, respectively, and varying densities ϕ as indicated on the bottom axis. Finally, the open squares show data for $L = 18$, $\phi = 0.7$, and different values of ε ranging between 10^{-4} and 10^{-1}.

in Fig. 2 we show that the data discussed in [12] are also well described by the following equation

$$\nu = -B \left(\frac{\phi}{\phi_{\mathrm{rcp}} - \phi} \right)^{1/2} \ln \left(\frac{4\,\varepsilon}{3} \right) \qquad (4)$$

with $B = 0.20 \pm 0.02$.

In the following we explore in how far the prediction, Eq. (3), complemented with the expression, Eq. (4), provides a faithful description of the arrest stress in systems where the shear rate, $\dot{\gamma}$, is prescribed.

III. NUMERICAL METHOD

We numerically solve Newton's equation of motion of a 1:1 mixture of large and small disks moving in a two-dimensional domain of size $L \times L$ subjected to Lees-Edwards boundary conditions [19] that enforce a pre-scribed total shear, $L\dot{\gamma}$, in the system. All velocities and forces are calculated based on the appropriate representation of the flow in the two-dimensional plane that is obtained by properly unfolding the Lees-Edwards boundary conditions (*cf.* [19]). Crystalline ordering is prevented by considering a 1:1 mixture of large and small disks with a ratio $R_l/R_s = 1.4$ of their respective radii R_l and R_s [20]. The random-close packing limit of this mixture has been reported [20, 21] to be $\phi_{\mathrm{rcp}} = 0.84$. We assume a con-

stant mass per area, ρ, such that the mass of disk i is $m_i = \pi\rho R_i^2$.

A. Equations of motion

We adopt a fifth-order predictor-corrector Gear algorithm [19, 22] to solve Newton's equation of motion

$$m_i \frac{d^2\mathbf{r}_i}{dt^2} = \sum_{j \in \mathcal{N}(i)} \mathbf{e}_{ij}\, f_{ij}(r_{ij}) \;, \qquad (5)$$

where m_i and $\mathbf{r}_i$ are the mass and the center disk i, respectively, $\mathcal{N}(i)$ is the set of neighbors j interacting with i, the unit vector $\mathbf{e}_{ij}$ points from the center of disk i to the center of disk j, and f_{ij} is the force exerted by disk i on disk j. The latter force comprises a repulsion, and whenever applicable also the attractive force, F_c, modeling capillary bridges.

Mutual repulsion between the disks is modeled by the repulsive force

$$F_r(r_{ij}) = \begin{cases} C_{ij}(R_i + R_j - r_{ij})^{1/2} & \text{for } r_{ij} \le R_i + R_j \\ 0 & \text{else,} \end{cases}$$
$$(6a)$$

where r_{ij} is the Euclidean distance between he center of disk i and j. In the spirit of Hertz's contact law [23] we set

$$C_{ij} = C \left(\frac{R_i R_j}{R_i + R_j} \right)^{1/2} \qquad (6b)$$

in order to account for different disk radii. The global parameter C controls the hardness of the disks.

For the capillary bridges forces we engage the minimal capillary model proposed by Herminghaus in Ref. [24] in which the capillary force is constant, F_c, as the distance between granulates changes, and where it breaks at a distance s_c. This model has been shown to be well-suited for numerical simulations of wet granular materials [7, 8, 15, 25]. The force in this model is hysteretic: upon first approach there is no attractive force ($r_{ij} > R_i + R_j$); when the disks undergo collision ($r_{ij} \le R_i + R_j$) a constant (capillary) force F_c is activated, and the force persists until the disks separate by a (surface-to-surface) distance s_c ($r_{ij} \le R_i + R_j + s_c$). At that point, $r_{ij} = R_i + R_j + s_c$, the capillary bridge is removed (it 'ruptures'). There is no force acting between the disks again, until they undergo their next collision ($r_{ij} \le R_i + R_j$). Consequently, an energy $\epsilon = F_c s_c$ is dissipated after rupture of the capillary bridge.

Throughout this paper, we employ dimensionless rescaled quantities based on the capillary force, F_c, the mass density of the disks, ρ, and the average disk diameter D. Time, t, and mass, m, is hence measured in units $\tau \equiv \sqrt{\rho D^3/F_c}$, and $\mu \equiv \rho D^2$, respectively. Using these normalized quantities it is straightforward to normalize all physical quantities derived from mass, length and time, such as the local averages of disk velocities, components of the stress tensor, and the shear rate.

B. Data acquisition and analysis

For each parameter set we run 20 simulations over a fixed total strain of $\gamma_t = 10 \times L$. The choice to fix the total strain, rather than fixing the total simulation time, ensures that in the limit of very small flow rates we still sample a representative set of statistically uncorrelated disk configurations. We start to measure the physical quantities at the strain $\gamma = 4 \times L$ and take 150 shots over the rest of the simulations until $\gamma_t = 10 \times L$. Altogether these 150 configurations for 20 different runs provide 3000 independent snapshots for each considered parameter set. For each snapshot, we determine and store the components of the stress tensor, σ, as well as the average density, partial densities, and granular temperature evaluated in ten bands parallel to the shear.

The components of the stress tensor are calculated [12, 16, 26] by evaluating

$$
\begin{aligned}
\sigma_{\alpha\beta} &= \frac{1}{L^2} \sum_i m_i \left(v_{i,\alpha} - U_\alpha(\mathbf{x}_i) \right) \left(v_{i,\beta} - U_\beta(\mathbf{x}_i) \right) \\
&+ \frac{1}{L^2} \sum_{i<j} r_{ij,\alpha} \, F_{ij,\beta} \,.
\end{aligned}
\tag{7}
$$

In Eq. (7) $\alpha, \beta \in \{x, y\}$ denote the Cartesian components of the respective vectors or tensors. The stress tensor has two contributions: (I) the first term accounts for advective momentum transport, where , $\mathbf{v}_i$ is the velocity of the disk i, and $\mathbf{U}(\mathbf{x}_i)$ is the local drift velocity at the position $\mathbf{x}_i$ of disk i, i.e., the overall center-of-mass velocity of the disks with centers in an interval of width $L/10$ containing x_i. (II) the second term describes the contribution of the interaction forces between particles on the stress to the flux of linear momentum. In this contribution $\mathbf{r}_{ij}$ is the vector connecting the centers of disk i and j, and $\mathbf{F}_{ij}$ is the force exerted by the disk i on disk j. In the limit of small shear rates, $\dot{\gamma} \to 0$, one approaches creep flow, and the latter term in Eq. 7 always dominates the shear stresses.

For non-Newtonian fluids, the relationship between the shear stress, σ_{xy}, and the shear rate, $\dot{\gamma}$, is given by Herschel-Bulkley relation [27]:

$$
\sigma_{xy} = \sigma_a + K \times \dot{\gamma}^n
\tag{8}
$$

where, σ_a, is the arrest (yield) stress, K, is a constant, and, n, is the shear thinning exponent. According to a recent review by Bonn *et al.* [28], the shear thinning exponent is a material dependent parameter for which no universality has been found. Therefore, Eq. 8 would be a natural choice to be considered as a template function for experimental data fitting. However, we found out that when the shear thinning exponent, n, is variable, for large capillary energies, $\varepsilon > 0.05$, the fitting algorithm frequently takes very small exponents in the order of 10^{-1}. This very small exponent gives rise to a flow profile which is very steep near the origin. As a result
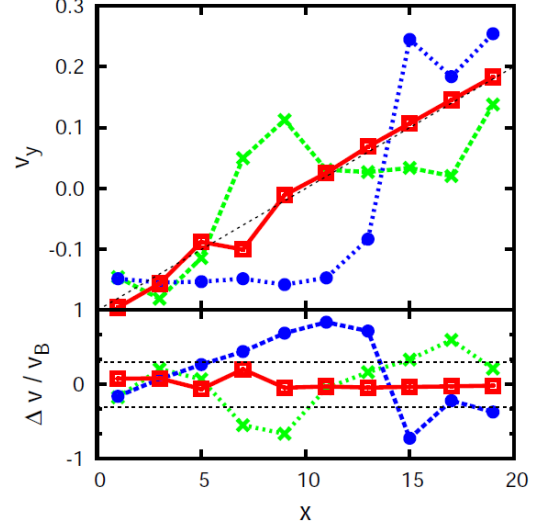

FIG. 3: (color online) The upper panel shows the mean center-of-mass velocity in ten stripes parallel to the flow for three shear profiles encountered in simulations for shear rate $\dot{\gamma} = 0.02$, system size $L = 20$, packing fraction $\phi = 0.82$, and capillary-bridge energy $\varepsilon = 0.1$. The lower panel shows the respective relative deviations from the ideal profile. The open red squares connected by a solid line mark a profile where the deviations from the mean profile are in the admissible bounds of $\pm 30\%$ that are indicated by thin black lines. Green crosses and blue circles, that are connected by broken lines in according color, show profiles where the system has formed a shear band.

of the sharp fall near the origin, it becomes more likely that the fitting algorithm grasps a negative offset. The negative offset corresponds to a negative arrest (yield) stress, σ_a, which is non-physical. In order to prevent this fitting failure, it is required that the final fitting flow profile should be smooth at the origin. This is guaranteed by enforcing $n > 1$. To be consistent, we choose a quadratic profile, $n = 2$, which is the most trivial choice given by the Bagnold scaling [17, 29].

C. Uniform shear profiles

In the analysis of the arrest stress we systematically disregard all the snapshots where the velocity profile deviates by more than a factor of 0.3 from the ideal linear case

$$
v_y(x) = \dot{\gamma} \left(x - \frac{L}{2} \right),
\tag{9}
$$

hence excluding phase-separated states (*cf.* Fig. 3). The ratio at which the snapshots are disregarded from further analysis strongly depends on the packing fraction, ϕ. The

higher the packing fraction, the lower the exclusion ratio. As an example, for $\phi = 0.52$, the rejection ratio is approximately $\simeq 72\%$, and for $\phi = 0.83$, it is about $\simeq 3\%$.

The lower panel of Fig. 3 shows the respective relative deviations from the ideal profile in order to exemplify the criterion for the selection of valid flow configurations. Flow configuration with deviations of the average flow velocities from the ideal profile (the thin dotted line in the upper panel of the figure) up to $\pm 30\%$ commonly appear as fluctuations on statistically uniform shear profiles: these flow configurations will enter the analysis of the arrest stress. On the other hand, larger fluctuations rapidly evolve into shear bands that are persistent in time—once they appear, they do not decay again. The green crosses and blue circles, that are connected by broken lines in according color in Fig. 3, show profiles where the system has formed a shear band. In that case the deviations lie noticeably outside the admissible range, and they persist: the system has phase separated into two domains of almost constant drift velocity; localizing the shear in narrow bands that lie at $5 \simeq x \simeq 10$ (green crosses) and $12 \simeq x \simeq 15$ (blue circles), respectively. These configurations must be excluded from the analysis because they show a region with a very low (often zero) number of capillary bridges, and hence anomalously low shear stress.

IV. RESULTS AND DISCUSSION

A. Shear-rate dependence of the arrest stress

In Fig. 4-Inset, we show the dependence of the components of the stress tensor on the shear rate $\dot{\gamma}$. The diagonal elements of the stress tensor, σ_{xx} and σ_{yy}, are depicted by red pluses and green crosses, respectively, and the blue stars show the off-diagonal element $\sigma_{xy} = \sigma_{yx}$. All curves show finite offsets at $\dot{\gamma} = 0$. The solid lines show the best fits by quadratic functions $\sigma_{\alpha\beta}(\dot{\gamma}) = a_{\alpha\beta} + b_{\alpha\beta}\dot{\gamma}^2$, where $a_{\alpha\beta}$ accounts for the non-vanishing stress at zero shear rates, and $b_{\alpha\beta}\dot{\gamma}^2$ is the Bagnold scaling expected to arise at large $\dot{\gamma}$ [17, 29]. In the main panel of Fig. 4, we verify this quadratic scaling for large $\dot{\gamma}$ by plotting the components of $\sigma - a$ on a double logarithmic scale. The offset of the off-diagonal element provides the arrest stress, $\sigma_a = a_{xy} = a_{yx}$. It is an intensive parameter of the system that does not depend on the system size. However, clearly, the components of a and b are functions of the density, ϕ, and the capillary energy, ε.

B. Parameter dependence of σ_a

Fig. 5-a demonstrates our data collapse according to Eq. (3) for the dependence of the arrest stress, σ_a, on the packing fraction, ϕ, for five different capillary energies, ε.
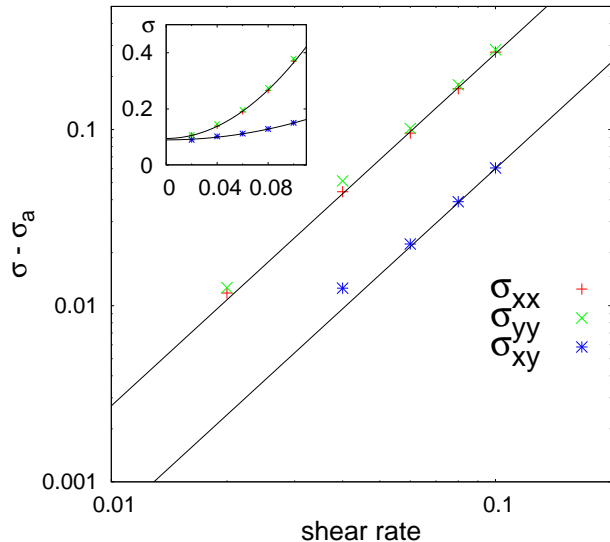

FIG. 4: (Inset) The shear rate, $\dot{\gamma}$, dependence of the components of the stress tensor, σ. The red pluses, green crosses, and blue stars show σ_{xx}, σ_{yy}, and $\sigma_{xy} = \sigma_{yx}$, respectively. The solid lines show the best fits by a quadratic function, $\sigma_{\alpha\beta}(\dot{\gamma}) = a_{\alpha\beta} + b_{\alpha\beta}\dot{\gamma}^2$, to the data where, $\sigma_{xx} = 0.095 + 27\dot{\gamma}^2$, $\sigma_{yy} = 0.097 + 27\dot{\gamma}^2$, and $\sigma_{xy} = 0.09 + 6\dot{\gamma}^2$. One can see that all the components of the stress tensor possess finite offsets at $\dot{\gamma} = 0$. This refers to a finite dynamic yield stress of wet granular materials for $\phi < \phi_{rcp}$. (Main Panel) Components of the stress tensor subtracted from their corresponding offsets, $\sigma - \sigma_a$, in a double logarithmic scale. In these simulations, the packing fraction is $\phi = 0.78$, capillary energy is $\varepsilon = 0.05$, and box length is $L = 20$.

For $0.6 \lesssim \phi \lesssim 0.8$ we find an excellent agreement between our data and the prediction $\sigma_a/(\phi\nu\varepsilon) = 1$ shown by the dotted line.

The data collapse is breaking down upon approaching the random close packing limit for values $\phi \gtrsim 0.8$. We expect that in this range the repulsive forces gives rise to an additional contribution to the stress, as observed in [17].

For $\phi \lesssim 0.6$ the values of σ_a systematically fall below the prediction, Eq. (3). This systematic error results from the choice $\sigma_a + b_a\dot{\gamma}^2$ of the function selected for extrapolating the $\dot{\gamma}$ dependence of σ_{xy} to small $\dot{\gamma}$: it does not account for the slight decrease of σ_{xy} for small values of $\dot{\gamma}$ in the regime where one expects shear banding (*cf.* for instance Fig. 1 of [17]). As shown in the main panel of Fig. 4 there always is a small mismatch of the simulation data and the fit function for small $\dot{\gamma}$. We still adopted the function $a + b\dot{\gamma}^2$ because it involves fewer parameters and results in a more robust fitting of our data. To within our numerical error margins the systematic error in the fit is negligible for $\phi \gtrsim 0.6$, where the dip becomes so minute that shear banding is no longer
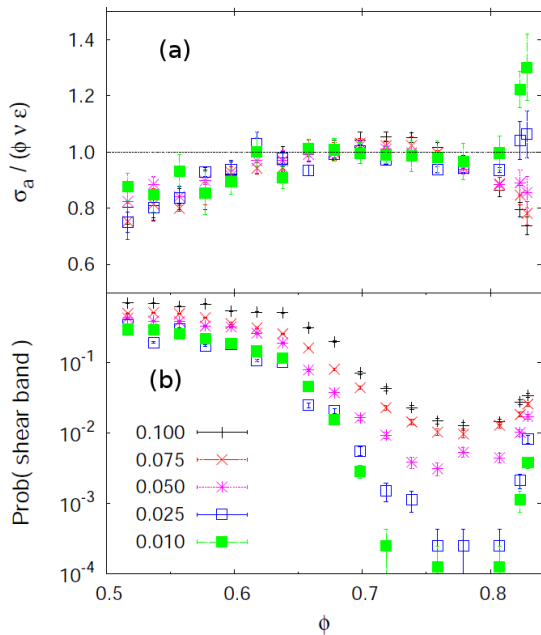
FIG. 5: **(a)** collapse of the data according to Eq. (3), which asserts that $\sigma_a/(\phi\nu\varepsilon)$ should be one (as indicated by the dotted line), as function of the packing fraction, ϕ, for $L = 20$ and five different capillary energies, ε, that are provided in the lower left corner of the panel-b. **(b)** The panel provides the probability to observe shear bands in the simulations. In the legend the corresponding capillary energy, ε, of each simulation is given.

encountered. On the other hand, for $\phi \lesssim 0.6$ the fit provides a value characterizing the minimum of $\sigma_{xy}(\dot{\gamma})$ rather than the asymptotic value for vanishing $\dot{\gamma}$. When this distinction becomes noticeable the system becomes prone to shear banding (Fig. 5-b).

V. CONCLUSIONS

We calculated the arrest stress, σ_a, characterizing the minimal value of $\sigma_{xy}(\dot{\gamma})$ for two-dimensional isotropic shear flows of wet granular disks by fitting the components of the stress tensor by a quadratic functions, $a+b\dot{\gamma}^2$. In the range $0.52 < \phi < 0.84$, all components of the stress tensor of wet granular materials approach non-trivial finite values for small $\dot{\gamma}$. The resulting offset value for the shear stress is of particular interest. In general it is different from the static yield stress, σ_y, that can be obtained [17] by considering the limit $\sigma_y = \lim_{\dot{\gamma}\to 0}\sigma_{xy}$. The latter characterizes the stress where a system at rest can start to flow. In the case of wet granular materials, the static yield stress is the force which is needed to break down the percolation network of capillary bridges. The former, *i.e.,* the dynamic yield stress, is the minimal value of the stress which is required to maintain the flow.

The prediction of the arrest stress is based on a bal-

ance of the power injected by increasing strain at a finite stress and the energy dissipation due to rupturing capillary bridges. For uniform shear this argument provides Eq. (3). This prediction has a single free parameter, the average number, ν, of bridges ruptures when particles pass each other in the flow. We have determined this number [12] in the context of a different flow, non-uniform shear flow driven by an external force field in periodic boundary conditions. Evoking universality of the number, ν, with respect to the cause of the flow provides a prediction of the arrest stress without adjustable parameters. The excellent data collapse shown in Fig. 5-a confirms the versatility of this approach to determine the arrest of flow [12, 15, 16], and the universality of ν as far the protocol of inducing the flow are concerned. The difference between our prediction, Eq. (3), and the numerical findings for $\phi \gtrsim 0.8$ have been associated to the emergence of contributions to the stress from repulsive forces when approaching random close packing. The systematic difference for $\phi \lesssim 0.6$ is due to a noticeable deviation of the arrest stress from the static yield stress. The larger the difference, the more likely the flow will phase separate into a state featuring shear bands (*cf.* Fig. 5-b).

Previous studies of far-from equilibrium transitions in wet granular materials have unraveled origins of these transitions to be either force- or energy-driven [8, 11]. For instance, for wet granulates in a Petri dish under vertical vibration, solid-to-fluid (fluid-to-gas) transition is force-driven (energy-driven). In sheared wet granular matter, the solid-to-fluid transition, whose threshold represents the static yield stress, has been shown to be of force-driven origin [30]

The present work complements and further substantiates the findings of previous studies [12, 15, 16] that attributed the fluid-to-solid transition in sheared wet granular systems is connected to a balance of the power injected by the forcing of the flow and the energy dissipation rate due to rupturing of capillary bridges in a plastic shear flow (energy-driven). This mechanism is fundamentally connected to the fact that wet granular materials have an inherent energy scale, the energy ε that is dissipated upon rupturing a capillary bridge [7, 24]. It will be interesting to explore the impact of this important distinction for other soft matter systems [17, 31, 32] where small attractive interactions and a dissipation due to transfer of kinetic energy into internal degrees of freedom of the system should admit a corresponding analysis of the arrest of flow.

This is in contrast to dry granular materials where the arrest of flow is expected to be controlled by frictional forces between the particles.

90004064.

[1] GDR MiDi, Eur. Phys. J. E **14**, 341 (2004).
[2] K. W. Desmond, U. Villa, M. Newey, and W. Losert, Phys. Rev. E **88**, 32202 (2013).
[3] F. da Cruz, S. Emam, M. Prochnow, J.-N. Roux, and F. Chevoir, Phys. Rev. E **72**, 21309 (2005).
[4] P. Jop, Y. Forterre, and O. Pouliquen, Nature **441**, 727 (2006).
[5] R. Delannay, M. Louge, P. Richard, N. Taberler, and A. Valance, Nature Mater. **16**, 99 (2007).
[6] Y. Forterre and O. Pouliquen, Annu. Rev. Fluid Mech. **40**, 1 (2008).
[7] M. Scheel, D. Geromichalos, and S. Herminghaus, J. Phys. Cond. Mat. **16**, S4213 (2004).
[8] A. Fingerle, K. Roeller, K. Huang, and S. Herminghaus, New J. Phys. **10**, 053020 (2008).
[9] K. Huang, M. Sohaili, M. Schröter, and S. Herminghaus, Phys. Rev. E **79**, 010301(R) (2009).
[10] K. Reller, J. P. D. Clewett, R. M. Bowley, S. Herminghaus, and M. R. Swift, Phys. Rev. Lett. **107**, 048002 (2011).
[11] S. Strauch and S. Herminghaus, Soft Matter **8**, 8271 (2012).
[12] S. H. E. Rahbari, J. Vollmer, S. Herminghaus, and M. Brinkmann, Phys. Rev. E **82**, 061305 (2010).
[13] K. Huang, M. Brinkmann, and S. Herminghaus, Soft Matter **8**, 11939 (2012).
[14] C. May, I. Rehberg, and K. Huang, Phys. Rev. E **88**, 062201 (2013).
[15] K. Roeller, J. Blaschke, S. Herminghaus, and J. Vollmer, J. Fluid Mech. **738**, 407 (2014), 1210.3247.
[16] S. H. E. Rahbari, M. Khadem-Maaref, and S. K. A. S. Yaghoubi, Phys. Rev. E **88**, 042203 (2013).
[17] E. Irani, P. Chaudhuri, and C. Heussinger, Phys. Rev. Lett. **112**, 188303 (2014).
[18] A. W. Lees and S. F. Edwards, J. Phys. C: Solid St. Phys. **5**, 1921 (1972).
[19] M. P. Allen and D. J. Tildesley, *Computer simulation of liquids* (Oxford UP, 1987).
[20] C. O'Hern, L. Silbert, A. Liu, and S. Nagel, Phys. Rev. E **68**, 011306 (2003).
[21] N. Xu, C. S. O'Hern, and L. Kondic, Phys. Rev. Lett. **94**, 016001 (2005).
[22] W. H. Press, S. A. Teukolsky, W. T. Vetterling, and B. P. Flannery, *Numerical Recipes in C++: The Art of Scientific Computing* (Cambridge University Press, Cambridge UK, 2002).
[23] T. Poeschel and T. Schwager, *Computational granular dynamics* (Springer, 2005).
[24] S. Herminghaus, Adv. Phys. **54**, 221 (2005).
[25] A. Fingerle and S. Herminghaus, Phys. Rev. Lett. **97**, 078001 (pages 4) (2006).
[26] G. Lois, A. Lemaitre, and J. M. Carlson, Phys. Rev. E **72**, 051303 (2005).
[27] W. Herschel and R. Bulkley, Kolloid Zeitschrift **39**, 291 (1926).
[28] D. Bonn, J. Paredes, M. M. Denn, L. Berthier, T. Divoux, and S. Manneville (2015), arXiv:1502.05281v1.
[29] D. Vøagberg, P. Olsson, and S. Teitel, Phys. Rev. Lett. **113**, 148002 (2014).
[30] S. H. E. Rahbari, J. Vollmer, S. Herminghaus, and M. Brinkmann, Europhys. Lett. **87**, 14002 (2009).
[31] G. Lois, J. Blawzdziewicz, and C. S. O'Hern, Phys. Rev. Lett. **100**, 028001 (2008).
[32] C. Pinaki, B. Ludovic, and B. Lydéric, Phys. Rev. E **85**, 021503 (2012).